

# Northumbria Research Link

Citation: Chen, Ling, Tian, Jiajun, Wu, Qiang and Yao, Yong (2023) Ultrahigh Sensitivity Temperature Sensor Based on Harmonic Vernier Effect. IEEE Sensors Journal, 23 (1). pp. 381-388. ISSN 1530-437X

Published by: IEEE

URL: <https://doi.org/10.1109/jsen.2022.3224719>  
<<https://doi.org/10.1109/jsen.2022.3224719>>

This version was downloaded from Northumbria Research Link:  
<https://nrl.northumbria.ac.uk/id/eprint/50907/>

Northumbria University has developed Northumbria Research Link (NRL) to enable users to access the University's research output. Copyright © and moral rights for items on NRL are retained by the individual author(s) and/or other copyright owners. Single copies of full items can be reproduced, displayed or performed, and given to third parties in any format or medium for personal research or study, educational, or not-for-profit purposes without prior permission or charge, provided the authors, title and full bibliographic details are given, as well as a hyperlink and/or URL to the original metadata page. The content must not be changed in any way. Full items must not be sold commercially in any format or medium without formal permission of the copyright holder. The full policy is available online: <http://nrl.northumbria.ac.uk/policies.html>

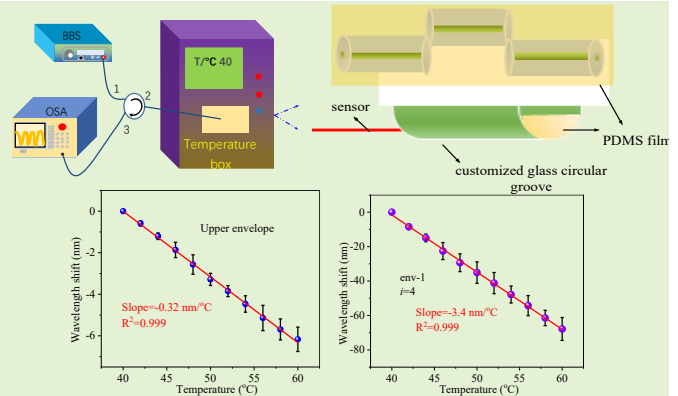
This document may differ from the final, published version of the research and has been made available online in accordance with publisher policies. To read and/or cite from the published version of the research, please visit the publisher's website (a subscription may be required.)

# Ultrahigh Sensitivity Temperature Fiber Sensor Based on Harmonic Vernier Effect

Ling Chen, Jiajun Tian\*, Qiang Wu, and Yong Yao

**Abstract**— A high-sensitivity and miniature open cavity Fabry–Perot interferometer (OCFPI) encapsulated with the polydimethylsiloxane (PDMS) film based on high-order harmonic Vernier effect is designed and experimentally investigated. To the best of our knowledge, PDMS is applied for the first time to fill the open cavity of Fabry–Perot interferometer to obtain high-temperature sensitivity. The resonant dip (peak) wavelength of the designed temperature sensor **monotonically** moves toward the shortwave direction as the temperature increases from 40°C to 60°C due to the effects of expansion and thermo–optic property of PDMS. The proposed OCFPI encapsulated with PDMS film provides the following excellent performance advantages. (1) Compared with traditional all-fiber air-cavity OCFPIs with temperature sensitivity of approximately 10 pm/°C, the proposed OCFPI sensor has a much higher temperature sensitivity of  $-3.4$  nm/°C at the temperature range of 40°C–60°C with a magnification factor ( $M$ -factor) of approximately 11 when order of harmonic Vernier effect  $i = 4$ . (2) The proposed OCFPI exhibits good reversibility during the heating and cooling processes, and the measured  $M$ -factor matches well with the theoretically calculated  $M$ -factor. (3) The proposed OCFPI shows excellent stability with maximum wavelength deviation of 0.567 nm (internal envelope based on a fourth-order harmonic Vernier effect) and 0.042 nm (upper envelope) within 450 min. (4) The proposed OCFPI is inexpensive, robust, easy to fabricate, and compact, which can be used in harsh environments. Therefore, it provides excellent potential in dynamic temperature measurement.

**Index Terms**— High-order harmonic Vernier effect;  $M$ -factor; open cavity FPI; PDMS film; temperature.



## I. INTRODUCTION

IN recent years, different types of optical-fiber temperature sensor structures have emerged and have been applied in all aspects of production and in everyday life [1–4]. Fabry–Perot interferometer (FPI) [5,6], Mach–Zehnder interferometer (MZI) [7], Michelson interferometer (MI) [8,9], side-polished fibers [10], long-period grating [11], fiber Bragg grating [12], and surface-plasmon resonance [13] sensors are the most common types of optical-fiber temperature sensors. Among these, Fabry–Perot (FP) sensors in optical fiber, as a promising sensing platform firstly proposed by the physicists Charles Fabry and Alfred Perot in 1897 [14], are the most commonly used structure owing to its low cost, simple fabrication, and ultra-compact in size [15,16]. Optical fiber based FPI is attracting wide research interests which includes intrinsic [17], and extrinsic FPI [18]. At present, two main types of optical-fiber temperature sensors are available, namely,

sensors coated with temperature-sensitive materials and those without coating. For sensors without a temperature-sensitive material coating, the refractive index (RI) and length of the optical-fiber change when the external temperature changes due to the thermal-optic and thermal-expansion effects of the silicon-dioxide material. For example, high-temperature MZI based on a few-mode fiber with a sensitivity of 48.2 pm/°C was proposed by Liu *et al.* [19]. A high-temperature sensor based on a hollow core fiber with a sensitivity of 33.4 pm/°C was reported by Liu *et al.* [20]. A high-temperature sensor based on reflective FPI with a low sensitivity of 20 pm/°C was proposed by Ge *et al.* [21]. To further improve the temperature sensitivity, temperature-sensitive materials were coated on the surface of the optical-fiber sensors, such as polydimethylsiloxane (PDMS), polymer–ultraviolet (UV) glue, and silicone. For example, an optical-fiber temperature sensor based on PDMS-covered microcavity with a sensitivity of 0.13 dB/°C was proposed by Iván Hernández-Romano *et al.* [22]. An MI structure based on suspended core fiber that was partially filled with polymer–UV glue with a temperature sensitivity of  $-164$  pm/°C was proposed by Mallik *et al.* [23]. A fiber-optic temperature sensor consisting of a multi-cladding special fiber coated with temperature-sensitive silicone with a temperature sensitivity of 240 pm/°C was reported by Pang *et al.* [24].

PDMS, a cheap, safe, and nontoxic polymer with good light

This work was supported in part by the National Natural Science Foundation of China (No. 61675055) and in part by the Shenzhen Science and Technology Program Project Nos. JCYJ20190806143818818 and GXWD20201230155427003-20200731103843002).

Ling Chen, Jiajun Tian, and Yong Yao are with the School of Electronics and Information Engineering, Harbin Institute of Technology, Shenzhen, Guangdong Province, 518055.

Qiang Wu is with the Faculty of Engineering and Environment, Northumbria University, Newcastle upon Tyne, U.K.

\*Corresponding author: Jiajun Tian; e-mail: tianjiajun@hit.edu.cn.

transmission, has been widely used in the temperature sensing field owing to its excellent linear thermal-expansion and thermo-optic effects. For example, a high-sensitivity-fiber temperature sensor based on MZI coated with a PDMS film whose corresponding temperature sensitivity was  $0.101 \text{ nm}/^\circ\text{C}$  was designed by Gong *et al.* [25]. The RI value of PDMS linearly varied with temperature, and it is expressed as  $n_{\text{PDMS}}(T) = -4.5 \times 10^{-4} \cdot T + 1.4176$ . Therefore, the RI value of PDMS linearly decreased as the temperature increased, and the thermo-optic coefficient of the PDMS was  $-4.5 \times 10^{-4} \text{ RIU}/^\circ\text{C}$  [26]. PDMS exhibits high structural flexibility owing to its low Young's modulus, which can solve the fragility defect of optical-fiber sensors. For example, an optical-fiber blood-pressure monitoring sensor based on a single-mode-multimode-single-mode structure encapsulated with PDMS to protect the fiber was proposed by Pang *et al.* [27]. In addition, PDMS demonstrates good biocompatibility and chemical inertness; thus, it is often applied as a microfluidic channel [28-31]. **Meanwhile, PDMS has also been utilized for chemical detection. For example, methane detection down to concentrations  $\sim 1\%$  in  $\text{N}_2$  has been demonstrated through the application of a ZIF-8/PDMS sensor coated on an optical fiber by Cao *et al.* [32].**

The harmonic Vernier effect was first proposed by A. D. Gomes in 2019 [33]. The outstanding advantage of the harmonic Vernier effect is its capability to break the limitation of the strict optical-path-length matching condition, which reduces the difficulty of preparing Vernier effect sensors with more considerable fabrication tolerance than the traditional Vernier effect. However, although the theoretical research on harmonic Vernier effect is relatively perfect, its practical application is relatively few. At present, the harmonic Vernier effect is only employed in gas-pressure [34], relative-humidity [35], and temperature [36,37] applications. More importantly, the reported temperature sensor based on the harmonic Vernier effect is only on the first order. Therefore, the large advantage of the harmonic Vernier effect is not fully exploited. In the present study, a high-order (fourth-order) harmonic Vernier effect is first applied to temperature measurement that demonstrates performance advantages.

This study proposes and has experimentally demonstrated a high-sensitivity open cavity FPI (OCFPI) encapsulated with the PDMS film based on a high-order harmonic Vernier effect. A short single-mode fiber (SMF) with a length of  $67 \mu\text{m}$  was spliced between lead-in SMF and  $290\text{-}\mu\text{m}$  SMF with a large lateral offset of  $90 \mu\text{m}$  to form a compact OCFPI configuration. The fabricated sensor was then encapsulated with the PDMS film in which a tightly connected open cavity filled with PDMS and a silica cavity with different free spectral ranges (FSRs) were used as the sensing and reference elements, respectively, to obtain a high-order harmonic Vernier effect. An ultrahigh temperature sensitivity of  $-3.4 \text{ nm}/^\circ\text{C}$  with a magnification factor ( $M$ -factor) of

approximately 11 was achieved based on the fourth-order harmonic Vernier effect. In addition, the temperature sensitivity, reproducibility, reversibility, and stability of the OCFPI were experimentally studied and discussed in detail.

## II. EXPERIMENTAL INVESTIGATION

### A. Fabrication of OCFPI and PDMS Film

Short-section SMF (Corning, ITU-T G.652.D) was sandwiched between SMFs with a large offset of  $90 \mu\text{m}$  using a fusion splicer (Fujikura 80 C) to form OCFPI. Three FPIs were fabricated with three reflected interfaces ( $M_1$ ,  $M_2$ , and  $M_3$ ), namely, open cavity (FPI<sub>1</sub>) with length  $L_1$ , silica cavity (FPI<sub>2</sub>) with length  $L_2$ , and hybrid cavity (FPI<sub>3</sub>) with length  $L_3$ . To generate the harmonic Vernier effect, the lengths of the open ( $L_1$ ) and silica ( $L_2$ ) cavities were precisely controlled and designed as  $67$  and  $290 \mu\text{m}$ , respectively. To ensure accuracy of the cleaved cavity length, the whole cleaving process was monitored using an optical microscope. The schematic diagram of the sensor structure and corresponding microscopic image are shown in Figs. 1(a) and (b), respectively. Then, the fabricated OCFPI sensor was encapsulated with a  $2\text{-mm}$ -thick PDMS film (which is a temperature-sensitive material) whose schematic diagram is shown in Fig. 1(c).

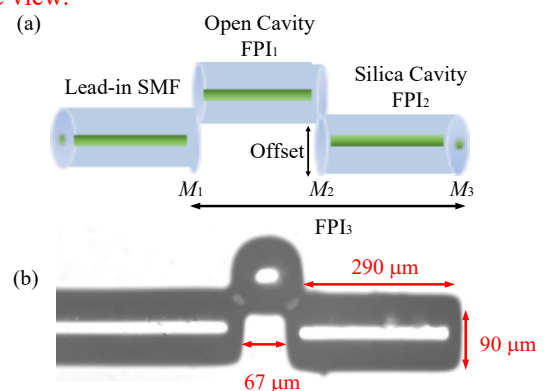
The detailed preparation and encapsulation steps of the PDMS film are described as follows.

1) A Sylgard 184 silicone elastomer base was thoroughly mixed with a curing agent at a ratio of 10:1 and stirred for 10 min. Subsequently, the mixed liquid was allowed to stand for 1 h to remove the bubbles generated during stirring.

2) The OCFPI was cleaned three times using ethanol and deionized water, and the sensor surface was kept clean.

3) The mixed liquids were poured into a customized C-shaped glass circular groove with a diameter of  $2 \text{ mm}$  where the cleaned optical-fiber sensor was placed at the middle of the groove. The schematic diagram is shown in Fig. 1(d).

4) The abovementioned customized C-shaped glass circular groove with an optical-fiber sensor was heated at  $70^\circ\text{C}$  for 12 h in a vacuum drying oven to completely cure the PDMS and obtain good stability. Figs. 1(e)–(g) show the images of the fabricated OCFPI encapsulated with the PDMS film (a transparent solid film) obtained by an optical microscope. **In Fig. 1, the image (e) is the top view and images (f) and (g) are the side view.**



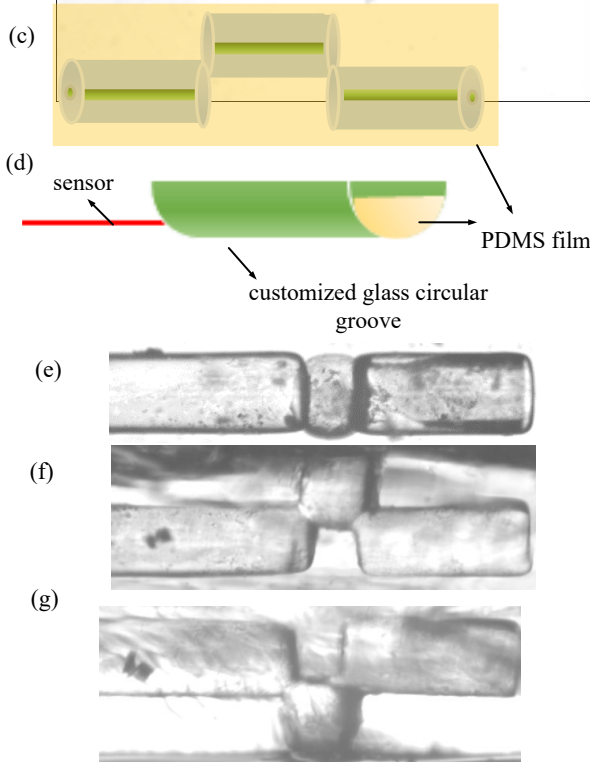


Fig. 1. (a) Schematic diagram of OCFPI. (b) Microscopic image of the sensor structure. (c) Schematic diagram of OCFPI encapsulated with PDMS. (d) Schematic diagram of the sensor encapsulated with a PDMS film with the customized glass circular groove. (e) Microscope image in X view. (f) and (g) Microscope image in Y view.

### B. Experimental Setup and Working Principle

Fig. 2 shows a schematic diagram of the experimental setup for the temperature measurement. The OCFPI encapsulated with the PDMS film was placed in a vacuum drying oven (DZT-6022, Shanghai Yiheng Scientific Instrument Co., Ltd). The fabricated temperature sensor was linked to a broadband light source [BBS (FiberLake ASE)] and the optical-spectrum analyzer [OSA (AQ6370C)] through a circulator. RI ( $n_{PDMS}$ ) of the PDMS filled within the FPI varied from 1.3996 to 1.3907 when the temperature increased from 40°C to 60°C [26]. The silica cavity was a reference cavity with RI = 1.45 ( $n_2$ ). The temperature change caused a change in RI ( $n_{PDMS}$ ) and the length in the open cavity ( $L_1$ ), resulting in the monotonical shift of the reflection spectrum. Therefore, the proposed OCFPI sensor could be used for temperature sensing.

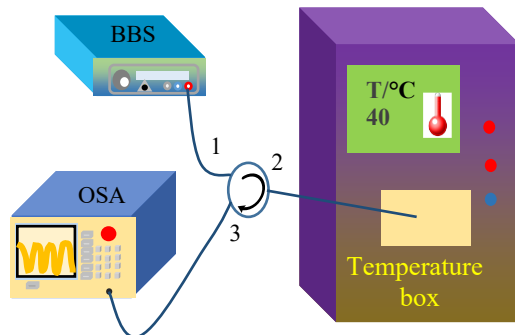


Fig. 2. Schematic diagram of the experimental setup for temperature sensing.

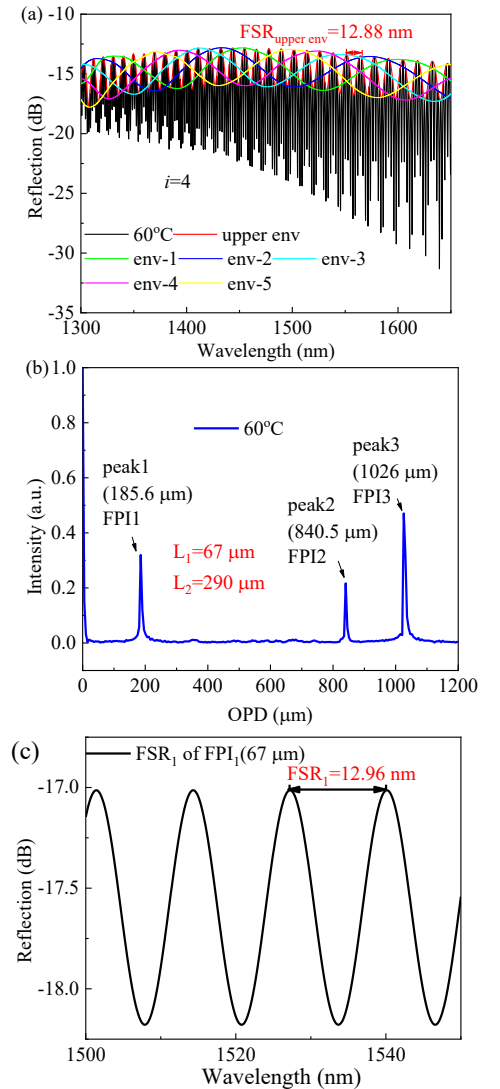
When the optical-path difference (OPL) of one interferometer increased by a multiple ( $i$  times) of OPL in the second interferometer, harmonics of the optical Vernier effect are generated [33]. For the  $i^{\text{th}}$ -order harmonic Vernier effect, (1) is satisfied, where  $i$  is an integer related to  $i^{\text{th}}$  OPL of the sensing cavity and the reference cavity expressed in (2) [38].  $\Delta$  is defined as the OPL detuning between the sensitive and reference cavities. The  $M$ -factor of the  $i^{\text{th}}$ -order harmonic Vernier effect is defined as the FSR ratio of the internal envelope to the spectrum of the sensitive cavity (open cavity) calculated by (3), where  $FSR_{\text{int}}$  and  $FSR_{\text{open}}$  are the FSRs of the internal envelope and FPI<sub>1</sub>, respectively [39].

$$n_2 L_2 = (i + 1) n_1 L_1 + \Delta \quad (1)$$

$$i = \left\lfloor \frac{n_2 L_2}{n_1 L_1} \right\rfloor - 1 \quad (2)$$

$$M = \frac{FSR_{\text{int}}}{FSR_{\text{open}}} = (i + 1) \frac{n_1 L_1}{\Delta} \quad (3)$$

$$FSR_{\text{open}} \approx \frac{\lambda_m^2}{2n_1 L_1} \quad FSR_{\text{silica}} \approx \frac{\lambda_m^2}{2n_2 L_2} \quad (4)$$



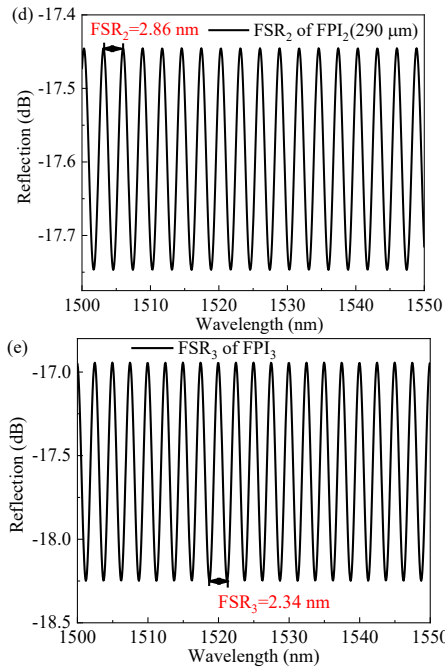


Fig. 3. (a) Spectra of the internal envelope based on the fourth-order harmonic Vernier effect and upper envelope of the fabricated OCFPI encapsulated with PDMS film at 60°C. (b) Spatial-frequency spectra based on linear-in-wavenumber resampling using fast Fourier transform in (a). (c) Filtering spectrum corresponding to peak 1. (d) Filtering spectrum corresponding to peak 2. (e) Filtering spectrum corresponding to peak 3.

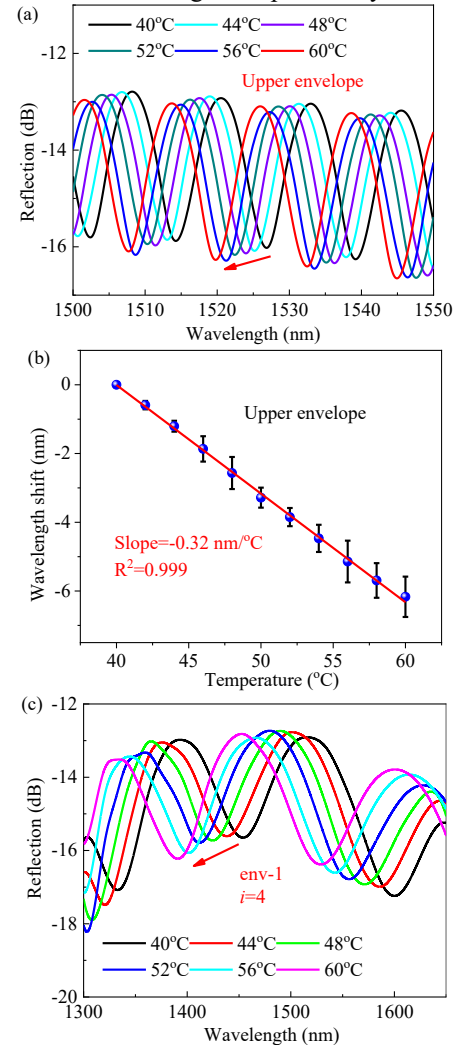
Fig. 3(a) shows the reflection spectrum of the OCFPI encapsulated with a PDMS film at 60°C, which is a typical spectrum of the fourth-order harmonic Vernier effect. This spectrum included five internal envelopes that are labeled as env-1, env-2, env-3, env-4, and env-5 using the internal envelope fitting method, which could be obtained from our previous work [25], and one upper envelope with FSR of 12.88 nm. The spatial-frequency spectra based on linear-in-wavenumber resampling using fast Fourier transform [Fig. 3(b)] could be obtained from Fig. 3(a), which contained three frequency-domain peaks (peak1, peak2, and peak3) that corresponded to three FP cavities, namely, FPI<sub>1</sub> (open cavity), FPI<sub>2</sub> (silica cavity), and FPI<sub>3</sub> (hybrid cavity) [40]. Fig. 3(b) shows that OPL of FPI<sub>2</sub> was 11 times that of FPI<sub>1</sub>, which satisfied (1). Therefore, the proposed OCFPI induced an optical harmonic Vernier effect. By substituting the specific OPD values of FPI<sub>1</sub> and FPI<sub>2</sub> (92.8 and 420.25 μm) into (1), we could observe that the optimal order of the designed OCFPI was four, and the corresponding detuning Δ value was -43.75 μm with *M*-factor of 11. The FSR of FPI<sub>1</sub>, FPI<sub>2</sub>, and FPI<sub>3</sub> (12.94, 2.84, and 2.38 nm, respectively) computed using (4) agreed well with the results (12.96, 2.86, and 2.34 nm, respectively) achieved by filtering peak 1, peak 2, and peak 3, respectively, as shown in Fig. 3(c) [41]. The reflected spectrum of the OCFPI shown in Fig. 3(a) was generated by the superposition of the three spectra [Figs. 3(c)–e)]. According to the previously reported literature [42], the upper envelope of the OCFPI was entirely determined by the single open cavity (FPI<sub>1</sub>), which confirmed that the upper envelope

of the OCFPI fully reflected the FPI<sub>1</sub> information. The information of the sensitive cavity (FPI<sub>1</sub>) could be directly obtained by tracking the upper envelope. Figs. 3(a) and (c) show that FSR of FPI<sub>1</sub> (12.96 nm) obtained by filtering peak1 was equal to the upper envelope FSR (12.88 nm), which conformed to the basic principle.

### III. EXPERIMENTAL RESULTS AND DISCUSSION

#### A. Temperature Measurement and Repeatability

During the heating process, the temperature gradually increased from 40°C to 60°C at a step change of 2°C, and each temperature value was stabilized for 1 h. Fig. 4(a) shows that the fitted upper envelope of the OCFPI reflection spectrum exhibited a significant blue shift as the temperature increased from 40°C to 60°C. The main reason for this shift was the RI change in PDMS from 1.3996 to 1.3907 as the temperature increased from 40°C to 60°C [26]. The excellent linear relationship between the wavelength shift of the upper envelope and temperature is shown in Fig. 4(b). The measurement was repeated three times to study the repeatability of the temperature sensor. The average temperature sensitivity was -0.32 nm/°C with a linear correlation coefficient of 0.999. We could observe that the proposed OCFPI exhibited good repeatability.



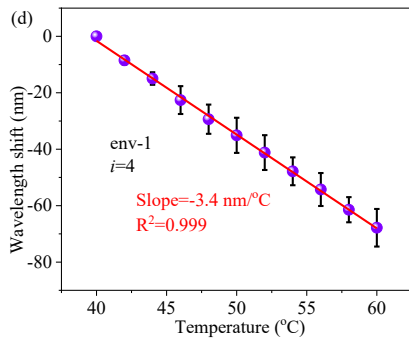


Fig. 4. Heating process. (a) Spectral response of the OCFPI upper envelope as the temperature varies from 40°C to 60°C. (b) Measured wavelength shift and calculated sensitivity of the OCFPI upper envelope versus temperature for three times. (c) Spectral response of OCFPI env-1 based on the fourth-order harmonic Vernier effect as the temperature varies from 40°C to 60°C. (d) Measured wavelength shift and calculated sensitivity of OCFPI env-1 based on the fourth-order harmonic Vernier effect versus temperature for three times.

To verify whether the designed OCFPI achieved sensitivity amplification, the spectral response of the temperature sensor was analyzed by tracking env-1 based on the fourth-order harmonic Vernier effect. Figs. 4(c) and (d) show that the spectrum of env-1 based on the fourth-order harmonic Vernier effect demonstrated a monotonic blue shift tendency when the temperature increased from 40°C to 60°C with an average temperature sensitivity of  $-3.4 \text{ nm}/^\circ\text{C}$  and a good linear correlation coefficient of 0.999, respectively. The temperature sensitivity of the OCFPI upper envelope was equal to that of the single sensitive cavity (FP11). Therefore,  $M$ -factor of the OCFPI was calculated to be approximately 11, which was consistent with the theoretical calculation using (3). The temperature sensitivity of OCFPI improved from  $-0.32$  to  $-3.4 \text{ nm}/^\circ\text{C}$  with the help of the fourth-order harmonic Vernier effect, which was much higher than the traditional internal- and external-cavity FPIs with low sensitivity of  $3.5 \text{ pm}/^\circ\text{C}$  [42].

### B. Reversibility of OCFPI

Reversibility, as an important parameter, characterizes the performance of temperature sensors. To verify the OCFPI reversibility, the temperature was designed to decrease from 60°C to 40°C at a step change of 2°C for three times. The spectral response of the upper envelope during the cooling process is shown in Fig. 5(a). The spectrum evidently moved toward the long-wave direction when the temperature decreased from 60°C to 40°C. The average temperature sensitivity of the upper envelope was  $-0.325 \text{ nm}/^\circ\text{C}$  with a good linearity of 0.999, as shown in Fig. 5(b), which was consistent with the heating process ( $-0.32 \text{ nm}/^\circ\text{C}$ ). The spectra of tracked env-1 based on the fourth-order harmonic Vernier effect are shown in Fig. 5(c), which indicated an obvious red shift as the temperature decreased from 60°C to 40°C. The average temperature sensitivity was  $-3.42 \text{ nm}/^\circ\text{C}$ , as shown in Fig. 5(d). We could observe that the OCFPI coated with PDMS demonstrated excellent reversibility and repeatability. The  $M$ -factor value of the OCFPI based on the fourth-order harmonic Vernier effect in the experiment was approximately

11, which agreed well with the heating process and theoretically calculated value using (3).

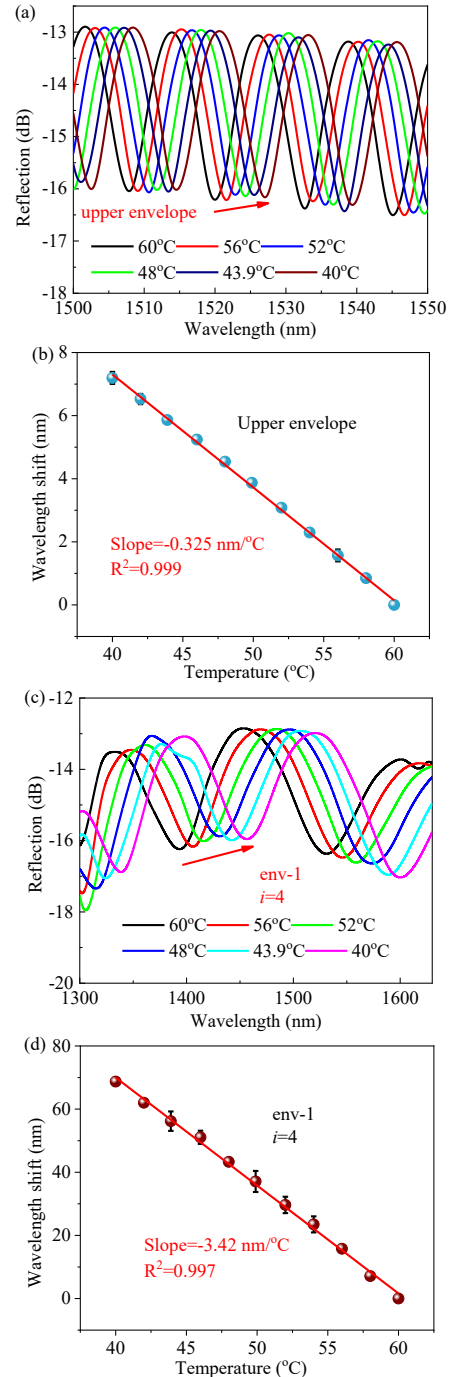


Fig. 5. Cooling process. (a) Spectral response of the fitted upper envelope as the temperature varies from 60°C to 40°C. (b) Measured wavelength shift and calculated sensitivity of the OCFPI upper envelope versus temperature for three times. (c) Spectral response of OCFPI env-1 based on the fourth-order harmonic Vernier effect as the temperature varies from 60°C to 40°C. (d) Measured wavelength shift and calculated sensitivity of OCFPI env-1 based on the fourth-order harmonic Vernier effect versus temperature for three times.

### C. Stability of OCFPI

In addition, stability, as an important indicator, is used to determine the performance of temperature sensors. The OCFPI stability was experimentally tested for 450 min when the temperature remained at 40°C and 60°C. The experimental

data of the spectral monitoring were recorded every 30 min for every experimental data. The spectral responses of the tracked upper envelope and env-1 based on the fourth-order harmonic Vernier effect at 0 and 450 min are shown in Fig. 6(a) when the temperature values were 40°C and 60°C, respectively. However, no obvious wavelength shift was observed in the spectrum (within 450 min of continuous monitoring). The summarized wavelength deviation of the temperature sensor within 450 min is shown in Fig. 6(c). The maximal dip wavelength fluctuations of the upper envelope and env-1 based on the fourth-order harmonic Vernier effect were 0.042 and 0.567 nm, respectively, which revealed that the proposed temperature sensor had a relatively good stability. Fig. 6(c) shows that the wavelength shifts of env-1 based on the fourth-order harmonic Vernier effect was very much larger than that of the upper envelope at the same temperature interval. More importantly, the wavelength shifts of env-1 based on the fourth-order harmonic Vernier effect (72.5 nm) from 40°C to 60°C was approximately 11 times that of the upper envelope (6.9 nm), which was in accordance with the theoretical calculated value of the  $M$ -factor and the aforementioned experimental results. This result proved that the proposed temperature sensor could provide good performance advantages that are extremely suitable for applications in environments that require high stability.

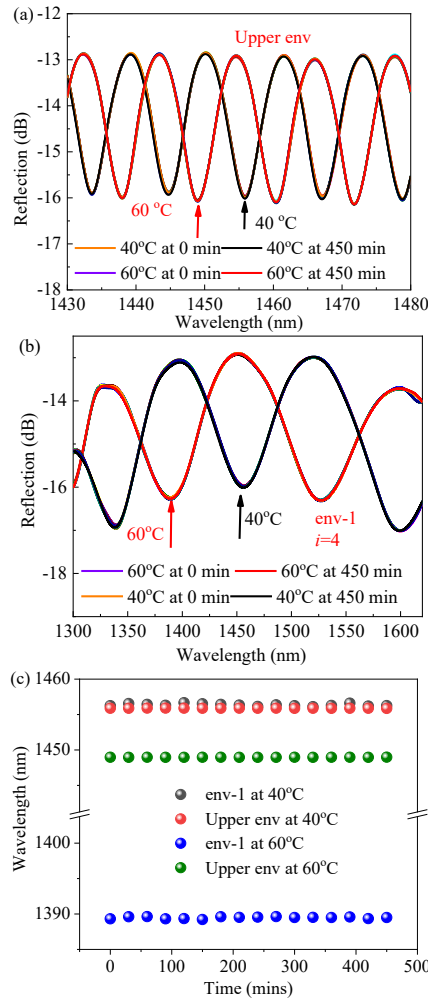


Fig. 6. Stability test. (a) Spectral response of the upper envelope at 0 and 450 min when the temperature is stable at 40°C and 60°C. (b) Spectral response of env-1 based on the fourth-order harmonic Vernier effect at 0 and 450 min when the temperature is stable at 40°C and 60°C. (c) Stability test: measured wavelength shifts of the upper envelope and env-1 based on the fourth-order harmonic Vernier effect within 450 min.

TABLE 1  
PERFORMANCE COMPARISON OF DIFFERENT OPTICAL-FIBER TEMPERATURE-SENSOR STRUCTURES

Fiber Structure	Materials	Sensitivity (dB/°C or nm/°C)	Operational complexity	References
air-microbubble FPI	PDMS	2.7035 nm/°C	complex	[43]
Dual HCF-based FPI	No	-0.481 nm/°C	simple	[44]
peanut-shape structure	No	0.073 nm/°C	simple	[45]
few-mode dual-concentric-core fiber	No	52.79 pm/°C	simple	[46]
D-shaped polarization-maintaining fiber	No	130 pm/°C	simple	[47]
singlemode-coreless-singlemode (SCS) fiber structure-based fiber ring cavity laser	No	11 pm/°C	simple	[48]
multimode microfiber-based dual MZI	No	-0.193 nm/°C	complex	[49]
Etched PCF FPI Micromachined by a 157-nm Laser	No	0.45 pm/°C	complex	[50]
Batch-producible all-silica fiber-optic FP sensor	No	0.435 nm/°C	complex	[51]
<b>OCFPI</b>	<b>PDMS</b>	<b>-3.4 nm/°C</b>	<b>simple</b>	<b>Proposed in this paper</b>

Table 1 lists the summary of the temperature sensitivity and difficulty of preparation of the different optical-fiber temperature sensors. By comparison, the sensitivity of our proposed sensor is higher than those listed in Table 1.

#### IV. CONCLUSION

This work has proposed and experimentally studied OCFPI encapsulated with the PDMS film based on the high-order harmonic Vernier effect. First, the OCFPI sensor was designed to be 67 and 290 μm according to the principle of the harmonic Vernier effect. The OCFPI sensor was encapsulated with the PDMS film, and the corresponding reflection spectral components were analyzed in detail using fast Fourier transform. The OCFPI encapsulated with the PDMS film was

placed in a vacuum drying oven for temperature measurement. The spectral response of the OCFPI encapsulated with the PDMS film exhibited a significant blue shift when the temperature increased from 40°C to 60°C for three times. The average temperature sensitivities of env-1 based on the fourth-order harmonic Vernier effect and upper envelope were  $-0.32$  and  $-3.4$  nm/°C, respectively, with an  $M$ -factor value of 11 and a small error bar. In addition, the proposed temperature sensor demonstrated good reversibility and repeatability with a similar temperature sensitivity during the heating and cooling processes. Furthermore, the stability of the OCFPI encapsulated with the PDMS film based on a high-order harmonic Vernier effect was experimentally investigated. The maximum wavelength shifts of env-1 based on the fourth-order harmonic Vernier effect and upper envelope were only 0.567 and 0.042 nm, respectively, within 450 min, which proved that the proposed temperature sensor can provide excellent stability.

## REFERENCES

- [1] J. Dakin and B. Culshaw, *Optical Fiber Sensors: Principles and Components*. Norwood: Artech House, 1988.
- [2] B. Culshaw and J. Dakin, *Optical Fiber Sensors: Systems and Applications*. Norwood, MA: Artech House, 1989.
- [3] K. T. V. Grattan and B. T. Meggitt, *Optical Fiber Sensor Technology: Fundamentals*. Norwell, MA: Kluwer, 2000.
- [4] K. T. V. Grattan and B. T. Meggitt, Eds., *Optical Fiber Sensor Technology: Advanced Applications*. Dordrecht, The Netherlands: Kluwer, 2000, pp. 79–187.
- [5] Y. Hu, H. Wei, Z. Ma, L. Zhang, F. Pang, and T. Wang, “Microbubble-based optical fiber Fabry-Perot sensor for simultaneous high-pressure and high-temperature sensing,” *Opt. Express*, vol. 30, no. 19, pp. 33639–33651, Sep 2022.
- [6] C. Zhou, Q. Zhou, B. Wang, J. Tian, and Y. Yao, “High-sensitivity relative humidity fiber-optic sensor based on an internal – external Fabry – Perot cavity Vernier effect,” *Opt. Express*, vol. 29, no. 8, pp. 11854–11868, Apr 2021.
- [7] L. Ma et al., “High-performance all-fiber Mach-Zehnder interferometer based on D-shaped two-mode fiber coated with polydimethylsiloxane for temperature sensing,” *Opt. Fiber Technol.*, vol. 71, May, 2022, Art. no. 102924.
- [8] Y. Zhao et al., “Ultrasensitive temperature sensor with Vernier-effect improved fiber Michelson interferometer,” *Opt. Express*, vol. 29, no. 2, pp. 1090–1101, Jan 2021.
- [9] D. Wu, T. Zhu, and M. Liu, “A high temperature sensor based on a peanut-shape structure Michelson interferometer,” *Opt. Commun.*, vol. 285, no. 24, pp. 5085–5088, Aug 2012.
- [10] C. Teng et al., “Double-side polished U-shape plastic optical fiber based SPR sensor for the simultaneous measurement of refractive index and temperature,” *Opt. Commun.*, vol. 525, Aug, 2022, Art. no. 128844.
- [11] K. Fukushima, A. Wada, S. Tanaka, and F. Ito, “EDF laser temperature sensor using double-pass cascaded-chirped long-period fiber grating in sigma-cavity configuration,” *Opt. Commun.*, vol. 508, Aug, 2022, Art. no.127713.
- [12] F. Esposito, S. Campopiano, and A. Iadicicco, “Miniaturized strain-free fiber Bragg grating temperature sensors,” *IEEE Sens. J.*, vol. 22, no. 17, pp. 16898–16903, Sep 2022.
- [13] N. Luan, R. Wang, W. Lv, Y. Lu, and J. Yao, “Surface plasmon resonance temperature sensor based on photonic crystal fibers randomly filled with silver nanowires,” *Sensors*, vol. 14, no. 9, pp. 16035–16045, Aug 2014.
- [14] C. Fabry and A. Perot, “Sur les franges des lames minces argentées et leur application à la mesure de petites épaisseurs d’air,” *Ann. Chim. Phys.*, vol. 12, pp. 459–501, 1897.
- [15] C. E. Lee and H. F. Taylor, “Sensors for smart structures based upon the Fabry–Pérot interferometer,” in *Fiber Optic Smart Structures*, E. Udd, Ed. New York: Wiley, 1995, pp. 249–269.
- [16] T. Zhu, D. Wu, M. Liu, and D. W. Duan, “In-line fiber optic interferometric sensors in single-mode fibers,” *Sensors (Switzerland)*, vol. 12, no. 8, pp. 10430–10449, Aug 2012.
- [17] R. Cao, Y. Yang, M. Wang, X. Yi, J. Wu, S. Huang, and K.P. Chen, “Multiplexable intrinsic Fabry – Perot interferometric fiber sensors for multipoint hydrogen gas monitoring,” *Opt. Lett.*, vol. 45, no. 11, pp. 3163–3166, Jun 2020.
- [18] W. Xiong et al., “Sensitivity enhanced fiber optic hydrophone based on an extrinsic Fabry-Perot interferometer for low-frequency underwater acoustic sensing,” *Opt. Express*, vol. 30, no. 6, pp. 9307–9320, Mar 2022.
- [19] J. Liu et al., “Mach-Zehnder Interferometer for High Temperature (1000 °C) Sensing Based on a Few-Mode Fiber,” *Photonic Sensors*, vol. 11, no. 3, pp. 341–349, Jun 2021.
- [20] D. Liu et al., “Hollow Core Fiber Based Interferometer for High-Temperature (1000 °C) Measurement,” *J. Light. Technol.*, vol. 36, no. 9, pp. 1583–1590, May 2018.
- [21] J. Kou, J. Feng, L. Ye, F. Xu, and Y. Lu, “Miniaturized fiber taper reflective interferometer for high temperature measurement,” *Opt. Express*, vol. 18, no. 13, pp. 14245–14250, Jun 2010.
- [22] I. Hernández-Romano et al., “Optical fiber temperature sensor based on a microcavity with polymer overlay,” *Opt. Express*, vol. 24, no. 5, pp. 5654–5661, Mar 2016.
- [23] S. Wang et al., “Fiber tip Michelson interferometer for temperature sensing based on polymer-filled suspended core fiber,” *Opt. Laser Technol.*, vol. 141, Apr 2021, Art. no. 107147.
- [24] F. Pang et al., “Special optical fiber for temperature sensing based on cladding-mode resonance,” *Opt. Express*, vol. 16, no. 17, pp. 12967–12972, Aug 2008.
- [25] J. Gong et al., “High sensitivity fiber temperature sensor based PDMS film on Mach-Zehnder interferometer,” *Opt. Fiber Technol.*, vol. 53, Oct, 2019, Art. no. 102029.
- [26] Z. Zhu, L. Liu, Z. Liu, Y. Zhang, and Y. Zhang, “Surface-plasmon-resonance-based optical-fiber temperature sensor with high sensitivity and high figure of merit,” *Opt. Lett.*, vol. 42, no. 15, pp. 2948–2951, Jul 2017.
- [27] Y. N. Pang et al., “Singlemode-Multimode-Singlemode Optical Fiber Sensor for Accurate Blood Pressure Monitoring,” *J. Light. Technol.*, vol. 40, no. 13, pp. 4443–4450, Jul 2022.
- [28] C. Zhou, S. Liang, Y. Li, H. Chen, and J. Li, “Fabrication of sharp-edged 3D microparticles via folded PDMS microfluidic channels,” *Lab Chip*, vol. 22, no. 1, pp. 148–155, Nov 2022.
- [29] J. Cheon and S. Kim, “Fabrication and Demonstration of a 3D-printing/PDMS Integrated Microfluidic Device,” *Recent Prog. Mater.*, vol. 4, no. 1, pp. 1–1, Jan 2021.
- [30] N. Azizipour, R. Avazpour, M. Sawan, D. H. Rosenzweig, and A. Ajji, “Uniformity of spheroids-on-a-chip by surface treatment of PDMS microfluidic platforms,” *Sensors & Diagnostics*, vol. 1, no. 4, pp. 750–764, May 2022.
- [31] M. Zhang, J. Luo, R. Hu, and W. Lu, “Research on liquid flow behavior in deformed microfluidic channels made of PDMS material,” *J. Phys. Conf. Ser.*, vol. 2174, no. 1, Nov 2022, Art. no. 012057.
- [32] R. Cao et al., “Metal-organic framework functionalized polymer coating for fiber optical methane sensors,” *Sensors Actuators, B Chem.*, vol. 324, Jun 2020, Art. no. 128627.
- [33] A. D. Gomes et al., “Optical harmonic Vernier effect: A new tool for high performance interferometric fibre sensors,” *Sensors*, vol. 19, no. 24, pp. 1–18, Dec 2019.
- [34] X. Yang et al., “Simplified highly-sensitive gas pressure sensor based on harmonic Vernier effect,” *Opt. Laser Technol.*, vol. 140, February, 2021, Art. no. 107007.
- [35] C. Zhou, Y. Song, Q. Zhou, J. Tian, and Y. Yao, “Ultra-High-Sensitivity Humidity Fiber Sensor Based on Harmonic Vernier Effect in Cascaded FPI,” *Sensors*, vol. 22, no. 13, Jun 2022, Art. no. 4816.
- [36] S. Liu, G. Lu, D. Lv, M. Chen, and Z. Zhang, “Sensitivity

- enhanced temperature sensor with cascaded Sagnac loops based on harmonic Vernier effect,” *Opt. Fiber Technol.*, vol. 66, Jul, 2021, Art. no. 102654.
- [37] L. Xie, M. Chen, and Z. Zhang, “Simplified highly sensitive temperature sensor based on harmonic Vernier effect,” *Appl. Phys. B Lasers Opt.*, vol. 128, no. 8, pp. 1–7, Aug 2022.
- [38] A. D. Gomes, H. Bartelt, and O. Frazão, “Optical Vernier Effect: Recent Advances and Developments,” *Laser Photonics Rev.*, vol. 15, no. 7, pp. 1–16, May 2021.
- [39] A. D. Gomes et al., “Hollow microsphere combined with optical harmonic Vernier effect for strain and temperature discrimination,” *Opt. Laser Technol.*, vol. 127, Mar 2020, Art. no. 106198.
- [40] L. Chen, J. Li, J. Tian, Y. Bang, K. Tang, and Y. Yao, “Phase Demodulation Based on K-Space with High Sensitivity for Interferometric Fiber Sensor,” *IEEE Photonics J.*, vol. 14, no. 4, pp. 1–9, Aug 2022.
- [41] F. Li et al., “Plug-in label-free optical fiber DNA hybridization sensor based on C-type fiber Vernier effect,” *Sensors Actuators B Chem.*, vol. 354, Mar 2022, Art. no. 131212.
- [42] C. Zhou, Q. Zhou, C. He, J. Tian, Y. Sun, and Y. Yao, “Fiber Optic Sensor for Simultaneous Measurement of Refractive Index and Temperature Based on Internal-and- External-Cavity Fabry-Pérot Interferometer Configuration,” *IEEE Sens. J.*, vol. 21, no. 8, pp. 9877–9884, Feb 2021.
- [43] M. Chen, Y. Zhao, F. Xia, Y. Peng, and R. J. Tong, “High sensitivity temperature sensor based on fiber air-microbubble Fabry-Perot interferometer with PDMS-filled hollow-core fiber,” *Sensors Actuators, A Phys.*, vol. 275, pp. 60–66, Mar 2018.
- [44] C. L. Lee, H. Y. Ho, J. H. Gu, T. Y. Yeh, and C. H. Tseng, “Dual hollow core fiber-based Fabry-Perot interferometer for measuring the thermo-optic coefficients of liquids,” *Opt. Lett.*, vol. 40, no. 4, pp. 459–462, Feb 2015.
- [45] F. Yu, P. Xue, X. Zhao, and J. Zheng, “Investigation of an in-line fiber Mach-Zehnder interferometer based on peanut-shape structure for refractive index sensing,” *Opt. Commun.*, vol. 435, pp. 173–177, Nov 2018.
- [46] S. Yao, Y. Shen, Y. Wu, W. Jin, and S. Jian, “Strain-insensitive temperature sensor based on a few-mode dual-concentric-core fiber,” *Opt. Laser Technol.*, vol. 111, pp. 95–99, Sep 2019.
- [47] H. H. Qazi, A. B. Mohammad, H. Ahmad, and M. Z. Zulkifli, “D-shaped polarization maintaining fiber sensor for strain and temperature monitoring,” *Sensors*, vol. 16, no. 9, pp. 1–12, Sep 2016.
- [48] Z. B. Liu et al., “Axial strain and temperature sensing characteristics of the single-coreless-single mode fiber structure-based fiber ring laser,” *Appl. Phys. B Lasers Opt.*, vol. 117, no. 2, pp. 571–575, Jun 2014.
- [49] H. Luo, Q. Sun, Z. Xu, D. Liu, and L. Zhang, “Simultaneous measurement of refractive index and temperature using multimode microfiber-based dual Mach-Zehnder interferometer,” *Opt. Lett.*, vol. 39, no. 13, pp. 4049–4052, Jun 2014.
- [50] Z. Ran, S. Liu, Q. Liu, Y. Wang, H. Bao, and Y. Rao, “Novel high-temperature fiber-optic pressure sensor based on etched PCF F-P interferometer micromachined by a 157-nm laser,” *IEEE Sens. J.*, vol. 15, no. 7, pp. 3955–3958, Jul 2015.
- [51] J. Li et al., “Batch-producible all-silica fiber-optic Fabry-Perot pressure sensor for high-temperature applications up to 800 °C,” *Sensors Actuators A Phys.*, vol. 334, Jan 2022, Art. no. 113363.

**Ling Chen** is Ph.D candidate with the School of Electronics and Information Engineering, Harbin Institute of Technology, Shenzhen. Her research interest is fiber optic sensing.

**Jiajun Tian** received her Ph.D. degree from Harbin Institute of University, China. He is currently an associate Professor with Harbin Institute of Technology, Shenzhen, China. His main research interests include fiber optic sensing and fiber lasers.

**Qiang Wu** received the B.S. and Ph.D. degrees from Beijing Normal University and Beijing University of Posts and

Telecommunications, Beijing, China, in 1996 and 2004, respectively. He is an Associate Professor/Reader with Faculty of Engineering and Environment, Northumbria University, Newcastle Upon Tyne, United Kingdom. His research interests include optical fiber interferometers for novel fiber optical couplers and sensors, nanofiber, microsphere sensors for bio-chemical sensing, the design and fabrication of fiber Bragg grating devices and their applications for sensing, nonlinear fibre optics, surface plasmon resonant and surface acoustic wave sensors.

**Yong Yao** received the Ph.D. degree in School of Information Optoelectronics Technology, South China Normal University. He is currently a Professor at the Department of Electronic and Information Engineering, Harbin Institute of Technology, Shenzhen. His main research interests include optoelectronics and fiber lasers.